

Calculation of Airfoil Flutter by an Euler Method with Approximate Boundary Conditions

Chao Gao,* Shuchi Yang,† Shijun Luo,‡ and Feng Liu§
University of California, Irvine, Irvine, California 92697-3975

and
David M. Schuster¶

NASA Langley Research Center, Hampton, Virginia 23681

A numerical method is demonstrated for solving the steady and unsteady Euler equations on stationary Cartesian grids for the purpose of time-domain simulation of aeroelastic problems. Wall boundary conditions are implemented on nonmoving mean chord positions by assuming the airfoil being thin and undergoing small deformation, whereas the full nonlinear Euler equations are used in the flowfield for accurate resolution of shock waves and vorticity. The method does not require the generation of moving body-fitted grids and thus can be easily deployed in any fluid-structure interaction problem involving relatively small deformation of a thin body. The first-order wall boundary conditions are used in solving the full Euler equations, and the results are compared with the Euler solutions using the exact boundary conditions and known experimental data. It is shown that the first-order boundary conditions are adequate to represent airfoils of typical thicknesses with small deformation for both steady and unsteady calculations. Flutter boundaries are accurately predicted by this method for the Isogai wing model test case.

Nomenclature

b	= airfoil half-chord, = $c/2$
C_{dw}	= wave drag coefficient
C_l	= lift coefficient
C_m	= moment coefficient around quarter-chord, positive nose up
C_p	= pressure coefficient
c	= airfoil chord
E	= total specific energy
$(\mathbf{e}_x, \mathbf{e}_y)$	= unit vectors in (x, y) directions
$F(t, x)$	= instantaneous upper surface of airfoil
$f(x)$	= mean upper surface of airfoil
\mathbf{G}	= Euler flux vector
$G(t, x)$	= instantaneous lower surface of airfoil
$g(x)$	= mean lower surface of airfoil
H	= total specific enthalpy
h	= vertical displacement of elastic axis
(i, j)	= grid point index
M_∞	= freestream Mach number
n	= real time level
\mathbf{n}	= outer normal vector to cell surface
p	= pressure
\mathbf{q}	= velocity vector of fluid particle
\mathbf{q}_b	= velocity vector of the surface of control volume
R	= flux residual

R^*	= modified residual
Re	= Reynolds number based on airfoil chord
S	= surface of control volume
t	= real time
t^*	= pseudotime
U_∞	= freestream velocity
u, v	= x and y velocity components of fluid particle
u_b, v_b	= x and y components of grid velocity
V	= control volume
V_f	= flutter speed index
\mathbf{W}	= Euler conservative flow variable
x, y	= Cartesian coordinates
x_0	= x coordinate of the pivot point of airfoil pitching
α	= instantaneous angle of attack, deg
α_m	= mean angle of attack, deg
α_1	= instantaneous increment of angle of attack, deg
α_0	= amplitude of the pitching oscillation
γ	= ratio of specific heats
Δt	= real-time step
κ	= reduced frequency
μ	= mass ratio
ρ	= air density
τ	= structural dimensionless time, = $t\omega$
ω	= angular frequency

Received 10 October 2003; revision received 24 May 2004; accepted for publication 20 August 2004. Copyright © 2004 by the authors. Published by the American Institute of Aeronautics and Astronautics, Inc., with permission. Copies of this paper may be made for personal or internal use, on condition that the copier pay the \$10.00 per-copy fee to the Copyright Clearance Center, Inc., 222 Rosewood Drive, Danvers, MA 01923; include the code 0001-1452/05 \$10.00 in correspondence with the CCC.

*Visiting Associate Researcher, Department of Mechanical and Aerospace Engineering; currently Professor, Center for Aerodynamics Research and Development, Northwestern Polytechnical University, 710072 Xi'an, People's Republic of China.

†Postdoctoral Researcher, Department of Mechanical and Aerospace Engineering.

‡Researcher, Department of Mechanical and Aerospace Engineering.

§Professor, Department of Mechanical and Aerospace Engineering, Associate Fellow AIAA.

¶Senior Research Engineer, Aeroelasticity Branch, Associate Fellow AIAA.

I. Introduction

COMPUTATIONAL fluid dynamics (CFD) has proven to be a useful tool for the simulation and prediction of buffet, flutter, and limit-cycle-oscillation (LCO) phenomena of aeroelastic systems. Methods ranging from the linear doublet-lattice method¹ to methods that solve the Euler and the Navier–Stokes equations have been developed.^{2–13} Several recent review papers on computational aeroelasticity can be found in Refs. 14–17. Despite its limit in handling transonic and other nonlinear flows, the linear doublet-lattice method has been and is still the workhorse for actual design analysis in industry because of its efficiency in computer time and, perhaps equally important, the ease in setting up the computational problem. The Reynolds-averaged Navier–Stokes (RANS) methods encompass the most complete flow model short of large-eddy simulations or direct numerical simulations. However, time-domain RANS simulations for aeroelasticity problems at present demand

computational resources beyond those tolerable in a preliminary design environment. In addition, their usefulness is limited by uncertainties in turbulence modeling, grid resolution, and numerical damping effects, difficulties in grid generation and the transfer of displacements and aerodynamic forces between the structural and aerodynamic grids, and lack of fast and robust algorithms for deforming grids needed in the unsteady computations.^{5,16,18} In between the preceding two extremes, methods based on the various forms of the potential flow equation with boundary-layer corrections have shown good results for flutter simulations without the use of large computational resources and with less human work in setting up the computational problem including grid generation. Among such methods, the CAP-TSD^{19–21} code is widely known and used. The CAP-TSD code has many advantages over a full-fledged RANS code. These include 1) ease in generating a grid; 2) no need to do complex interpolation between the structural and CFD grids; 3) no need to have a moving grid; and 4) less demand on CPU time and memory.

Despite the use of vortex and entropy corrections, the potential flow assumption in CAP-TSD limits its applicability to irrotational flows with weak shocks. In addition, the small perturbation assumption is also applied to the field equation(s) and thus limits its applicability to only flows with small absolute angles of attack. Advances in computer speed and maturity of algorithms for the Euler equations have made the solution of the Euler equations a rather dependable and routine tool. Although the Euler equations cannot account for the viscous effects in the boundary layer, they are capable of resolving strong shocks and transporting vortices correctly. Because of the requirement of large computing resources by a Navier–Stokes code and also unresolved issues regarding accuracy of current numerical algorithms for the Navier–Stokes equations, the Euler equations strike a good balance between completeness of the flow model and computational efficiency.

To use the Euler equations but retain the ease in setting up a computational grid as in the CAP-TSD code, this paper develops an unsteady Euler solver for aeroelastic applications on stationary Cartesian grids through the use of approximate boundary conditions. The full Euler boundary conditions on the airfoil surface are replaced by their first-order expansions on the mean chord line of the airfoil for thin airfoils with small deformations, which is usually the case for flutter predictions for moving or deforming airfoils. The present method is distinguished from a traditional small-perturbations method in that the full Euler equations are used in the flowfield, which are not subject to the restriction of small perturbations in either the streamwise or transverse directions as is the case for the transonic small-perturbation potential equation. Although the thickness of the airfoil and the unsteady deformation from the mean positions are required to be small because of the use of the approximate boundary conditions, the mean angle of attack is not formally under the same small-perturbation restriction. By using these approximate boundary conditions, we can avoid the use of a body-fitted moving or deforming grid, which can be a rather time-consuming and nontrivial task for practical problems.¹⁶ The basic steady Euler solver is based on the finite volume code FLO52 by Jameson et al.²² An unsteady Euler/Navier–Stokes code based on FLO52 was developed by Liu and Ji.²³ This code is called NS83 and uses an implicit scheme with dual time stepping.²⁴ Details of the mathematical formulation of the approximate boundary conditions are presented along with their implementation in the finite volume code. Both steady and unsteady computations and coupled unsteady fluid-structure simulations are performed using the new Euler method with the proposed approximate boundary conditions. The results are compared with those obtained by FLO52 and NS83 with full boundary conditions and experimental data whenever available. Discussions and conclusions are finally drawn.

II. Euler Equations and Time-Accurate Scheme

Consider a moving and possibly deforming control volume (computational cell) V in two dimensions whose boundary S moves at velocity (u_b, v_b) . The two-dimensional unsteady Euler equations in conservative integral form in the Cartesian coordinate system (x, y)

for such a control volume are

$$\frac{\partial}{\partial t} \int_V \mathbf{W} dV + \int_S \mathbf{G} \cdot \mathbf{n} dS = 0 \quad (1)$$

where

$$\mathbf{W} = \begin{bmatrix} \rho \\ \rho u \\ \rho v \\ \rho E \end{bmatrix} \quad (2)$$

$$\mathbf{G} = \begin{bmatrix} \rho(\mathbf{q} - \mathbf{q}_b) \\ \rho u(\mathbf{q} - \mathbf{q}_b) + p\mathbf{e}_x \\ \rho v(\mathbf{q} - \mathbf{q}_b) + p\mathbf{e}_y \\ \rho E(\mathbf{q} - \mathbf{q}_b) + p(u\mathbf{e}_x + v\mathbf{e}_y) \end{bmatrix} \quad (3)$$

$$\mathbf{q} = u\mathbf{e}_x + v\mathbf{e}_y \quad (4)$$

$$\mathbf{q}_b = u_b\mathbf{e}_x + v_b\mathbf{e}_y \quad (5)$$

$$E = \frac{1}{\gamma - 1} \frac{p}{\rho} + \frac{1}{2}(u^2 + v^2) \quad (6)$$

Applying Eq. (1) to each cell in the mesh, we obtain a set of ordinary differential equations of the form

$$\frac{d}{dt}(\mathbf{W}_{i,j} V_{i,j}) + \mathbf{R}(\mathbf{W}_{i,j}) = 0 \quad (7)$$

where $V_{i,j}$ is the volume of the i, j cell and the residual $\mathbf{R}(\mathbf{W}_{i,j})$ is obtained by evaluating the flux integral in Eq. (1). Following Jameson,²⁴ we approximate the d/dt operator by an implicit backward difference formula of second-order accuracy in the following form (dropping the subscripts i, j for clarity):

$$(3/2\Delta t)\mathbf{W}^{n+1}V^{n+1} - (2/\Delta t)\mathbf{W}^nV^n + (1/2\Delta t)\mathbf{W}^{n-1}V^{n-1} + \mathbf{R}(\mathbf{W}^{n+1}) = 0 \quad (8)$$

Equation (8) can be solved for \mathbf{W}^{n+1} at each time step by solving the following steady-state problem for \mathbf{W} in a pseudotime t^* .

$$\frac{d\mathbf{W}}{dt^*} + \mathbf{R}^*(\mathbf{W}) = 0 \quad (9)$$

where

$$\mathbf{R}^*(\mathbf{W}) = \mathbf{R}(\mathbf{W}) + (3/2\Delta t)(\mathbf{W}V^{n+1}) - (2/\Delta t)(\mathbf{W}V^n) + (1/2\Delta t)(\mathbf{W}^{n-1}V^{n-1}) \quad (10)$$

Equation (9) is solved by an explicit time-marching scheme in t^* for which the local time stepping, residual smoothing, and multigrid techniques²² can be used to accelerate convergence to a steady state. Once the solution to Eq. (9) reaches a steady state, that is, when $d\mathbf{W}/dt^* \rightarrow 0$, \mathbf{W} is then assigned to \mathbf{W}^{n+1} .

In the present approximate method, the grid does not change with the time even for unsteady flow calculations. Thus, in the preceding equations the cell volume V satisfies $V^{n+1} = V^n = V^{n-1} = V$, and $\mathbf{q}_b = 0$.

III. Approximate Boundary Conditions

A thin airfoil slightly moving or deforming about its mean position is considered. The mean position of the airfoil chord lies on the horizontal axis x of the coordinate system between $x = 0$ and 1. The velocity of the incoming uniform freestream makes an angle α_m with the x axis. In the present paper, the airfoil is assumed to be of rigid shape but performs an oscillating motion around a fixed point on its chord line at $x = x_0$. The shape of the airfoil is described by $y = f(x)$ and $g(x)$ for its upper and lower surfaces, respectively. The instantaneous position of the airfoil is described by $y = F(t, x)$ and $y = G(t, x)$ for the upper and lower surfaces, respectively. The

flow is assumed inviscid. The boundary conditions on the upper surface of the airfoil at an instant t are

$$v(t, x, F) = u(t, x, F)F_x + F_t \quad (11)$$

where the subscripts x and t denote the partial derivatives with respect to x and t , respectively. Under the assumption $|F| \ll 1$, the first-order approximation of Eq. (11) on the x axis is

$$v(t, x, 0) = u(t, x, 0)F_x + F_t + \mathcal{O}(F) \quad (12)$$

where $\mathcal{O}(F)$ represents terms of the same order of magnitude as F or higher.

The boundary condition on the lower surface is treated similarly. The mean position of the leading edge of the airfoil is chosen as the origin of the coordinate system. If the leading edge is blunt, the boundary condition there is replaced by

$$u = 0 \quad (13)$$

At the sharp trailing edge of the airfoil, the pressures on the upper and lower surfaces should be equal to each other. In supercritical flow with adiabatic shock waves, the velocities and densities at the sharp trailing edge on the upper and lower surfaces might not be equal to each other. It is known that the Kutta condition at the sharp trailing edge is satisfied automatically in Euler calculations.

There are altogether four independent variables in the Euler equations (1), for example, ρ , u , v , and p . In addition to the boundary conditions of the velocity just given, more conditions are needed on the airfoil surfaces. The momentum differential equation in the outward normal direction \mathbf{n} is used, which gives

$$\mathbf{n} \cdot \left[\frac{\partial \mathbf{q}}{\partial t} + (\mathbf{q} \cdot \nabla) \mathbf{q} \right] = \mathbf{n} \cdot \left(-\frac{\nabla p}{\rho} \right) \quad (14)$$

On the upper surface of the airfoil, $y = F(t, x)$, the preceding equation becomes

$$p_y(t, x, F) = F_x p_x(t, x, F) - \rho(t, x, F) \times [F_{tt} + 2F_{tx}u(t, x, F) + F_{xx}u^2(t, x, F)] \quad (15)$$

The first-order approximation of the preceding equation is

$$p_y(t, x, 0) = F_x p_x(t, x, 0) - \rho(t, x, 0) \times [F_{tt} + 2F_{tx}u(t, x, 0) + F_{xx}u^2(t, x, 0)] + \mathcal{O}(F) \quad (16)$$

The corresponding equations on the lower surface of the airfoil are similarly derived.

In this paper, a rigid airfoil performing pitching oscillation about a point at $x = x_0$ on its mean chord is considered as an example. The instantaneous angle of the pitching rotation from the mean position is $\alpha_1(t)$, positive in clockwise direction. Given $f(x)$, the instantaneous ordinate of the upper surface $F(t, x)$ is expressed implicitly as follows:

$$F \cos \alpha_1 + (x - x_0) \sin \alpha_1 = f[x_0 + (x - x_0) \cos \alpha_1 - F \sin \alpha_1] \quad (17)$$

where the expression $x_0 + (x - x_0) \cos \alpha_1 - F \sin \alpha_1$ in the square brackets on the right-hand side of the equation is the argument of the function $f(x)$.

The five derivatives of $F(t, x)$ used in the first-order approximate boundary conditions can be evaluated exactly and are presented in Ref. 25 along with the following approximate expressions:

$$\begin{aligned} F_x &= f' - \tan \alpha_1 + \mathcal{O}(F^3), & F_{xx} &= f'' + \mathcal{O}(F^3) \\ F_t &= -\alpha_1'(x - x_0) \sec^2 \alpha_1 + \mathcal{O}(F^3) \\ F_{tx} &= -\alpha_1' \sec^2 \alpha_1 + \mathcal{O}(F^3) \\ F_{tt} &= -(x - x_0) \sec^2 \alpha_1 (\alpha_1'' + 2\alpha_1'^2 \tan \alpha_1) + \mathcal{O}(F^3) \end{aligned} \quad (18)$$

where the $'$ denotes differentiation of $f(x)$ and $\alpha_1(t)$ with respect to x and t , respectively.

IV. Numerical Implementation of the Boundary Conditions

Because the boundary of the airfoil is put on the x axis, $y = 0$, the computational grids can be taken to be rectilinear and parallel to the coordinate axes x and y . Two fictitious grid layers extending from the airfoil boundary outward are used in the finite volume method in order to calculate the flux vector \mathbf{G} and the second- and fourth-order artificial dissipation terms.

Figure 1 shows the two grid layers above the upper surface of $y = 0$ and the two fictitious grid layers extended from above. In the y direction, the two grids upward from $y = 0$ are named as 1 and 2, and the two grids downward from $y = 0$ are named as -1 and -2 . The upper surface $y = 0$ is denoted by 0. In the x direction the three consecutive grids are denoted by $i - 1$, i , and $i + 1$. Δx and Δy are the grid intervals in the x and y directions, respectively. All of the following expressions are derived for the same pseudotime level, and thus the independent variable t^* is dropped.

The density at the fictitious grid centers are evaluated by the linear extrapolation from inside the flowfield:

$$\rho_{i,-1} = 2\rho_{i,1} - \rho_{i,2} \quad (19)$$

$$\rho_{i,-2} = 2\rho_{i,-1} - \rho_{i,1} \quad (20)$$

The products of ρ and u at the fictitious grid centers are evaluated by the same linear extrapolation formula as those for ρ . Then the values of u at the fictitious grid centers are determined as the quotient of the local values of (ρu) and u . The value of u on the upper surface $y = 0$ is

$$u_{i,0} = \frac{1}{2}(u_{i,-1} + u_{i,1}) \quad (21)$$

Using the boundary condition (12), the value of v on the upper surface $y = 0$ is

$$v_{i,0} = F_{ti} + F_{xi}u_{i,0} \quad (22)$$

The values of v at the fictitious grid centers are evaluated as

$$v_{i,-1} = -v_{i,1} + 2v_{i,0} \quad (23)$$

$$v_{i,-2} = -v_{i,2} + 2v_{i,0} \quad (24)$$

The pressure at the fictitious grid centers are evaluated by using the boundary condition equation (16):

$$p_{i,-1} = p_{i,-2} = \max[(p_{i,1} - p_{y0}\Delta y), 0] \quad (25)$$

where

$$p_{y0} = F_{xi}p_{x0} - \rho_{i,0}(F_{tti} + 2F_{txi}u_{i,0}) - F_{xxi}(\rho_{i,0}u_{i,0})^2 / \rho_{i,0} \quad (26)$$

$$p_{x0} = (p_{i+1,1} - p_{i-1,1}) / (2\Delta x) \quad (27)$$

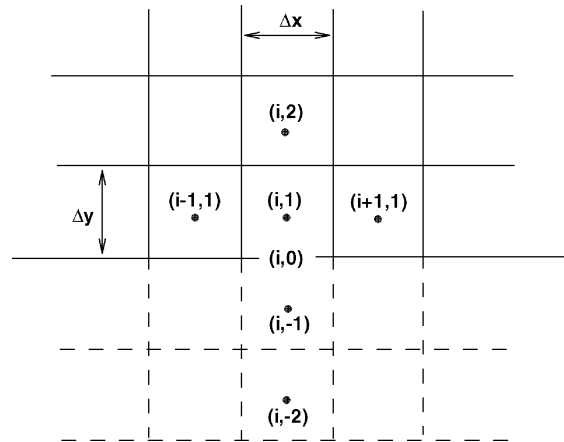


Fig. 1 Grids and fictitious grids.

$$\rho_{i,0}u_{i,0} = (\rho_{i,-1}u_{i,-1} + \rho_{i,1}u_{i,1})/2 \quad (28)$$

$$\rho_{i,0} = (\rho_{i,-1} + \rho_{i,1})/2 \quad (29)$$

Once the values of ρ , u , v , and p at the fictitious grid centers and on the boundary $y=0$ are determined, the other flow parameters can be evaluated by their definitions. The fictitious grid values of ρE are calculated as follows:

$$\rho_{i,-1}E_{i,-1} = \frac{p_{i,-1}}{\gamma - 1} + \frac{(\rho_{i,-1}u_{i,-1})^2 + (\rho_{i,-1}v_{i,-1})^2}{2\rho_{i,-1}} \quad (30)$$

$$\rho_{i,-2}E_{i,-2} = \rho_{i,-1}E_{i,-1} \quad (31)$$

V. Results and Discussion

A. Steady Flows

The steady inviscid compressible flows about three airfoils, NACA 0006, NACA 0012, and NACA 0015, are computed by FLO52 and the present approximate method at Mach number $M_\infty = 0.8$ and angles of attack α from 0 to 8 deg. FLO52 uses body-conforming curvilinear grids generated by conformal mapping. An O-type grid with 161×33 grid points is used for the benchmark calculations in this paper. The rectilinear grid used in the present approximate calculations consists of 141×67 grid points. For both grids, there are a total of 160 grid points on the airfoil surface, and the far-field boundaries are about 25 times the chord length away from the airfoil. Both grids are nonuniformly spaced so that more grid points are located in the neighborhood of the airfoil. Furthermore, grid points are also clustered near the leading and trailing edges. Figure 2 shows a close-up view of the nonuniform Cartesian grid near the leading edge of an NACA 0012 airfoil. The minimum grid sizes are $\Delta x = 0.00857$ chord and $\Delta y = 0.0118$ chord in the streamwise and transverse directions, respectively. A classical small-disturbance method suffers from a singularity problem at the blunt leading edge of an airfoil, where dy/dx is infinite. The streamwise grid size Δx at the leading edge of an airfoil cannot be made too small in a strict implementation of a small-perturbation boundary-condition method. The use of Eq. (13), which sets the streamwise flow velocity to zero, relieves this problem in the present method. However, a complete grid-convergence study is still not possible. A small Δx for a thick and blunt airfoil can cause local inaccuracies in the pressure distribution as will be discussed in the next paragraph. How small a Δx should be used depends on the particular airfoil and the flow conditions. All of the computations presented in this paper using the approximate boundary-condition method are performed on the same Cartesian grid discussed earlier.

The criterion for the convergence of the computations is that the maximum magnitude of the residuals be reduced by more than four orders of magnitude and is kept the same for both the present method and FLO52.

Figure 3 shows the comparisons of the pressure distributions over the airfoil NACA 0015 at $M_\infty = 0.8$ and $\alpha = 0, 4,$ and 8 deg with those obtained by FLO52. The pressure distributions of the present approximate calculations are evaluated on the chord line $y = 0$. It

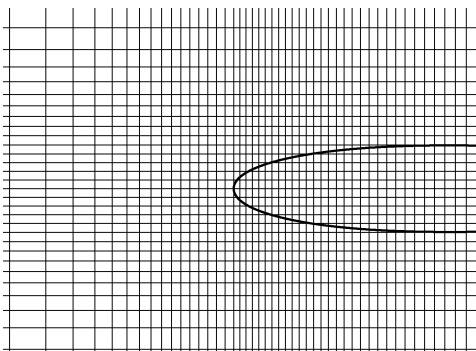


Fig. 2 Close-up view of the nonuniform Cartesian grid for the NACA 0012 airfoil.

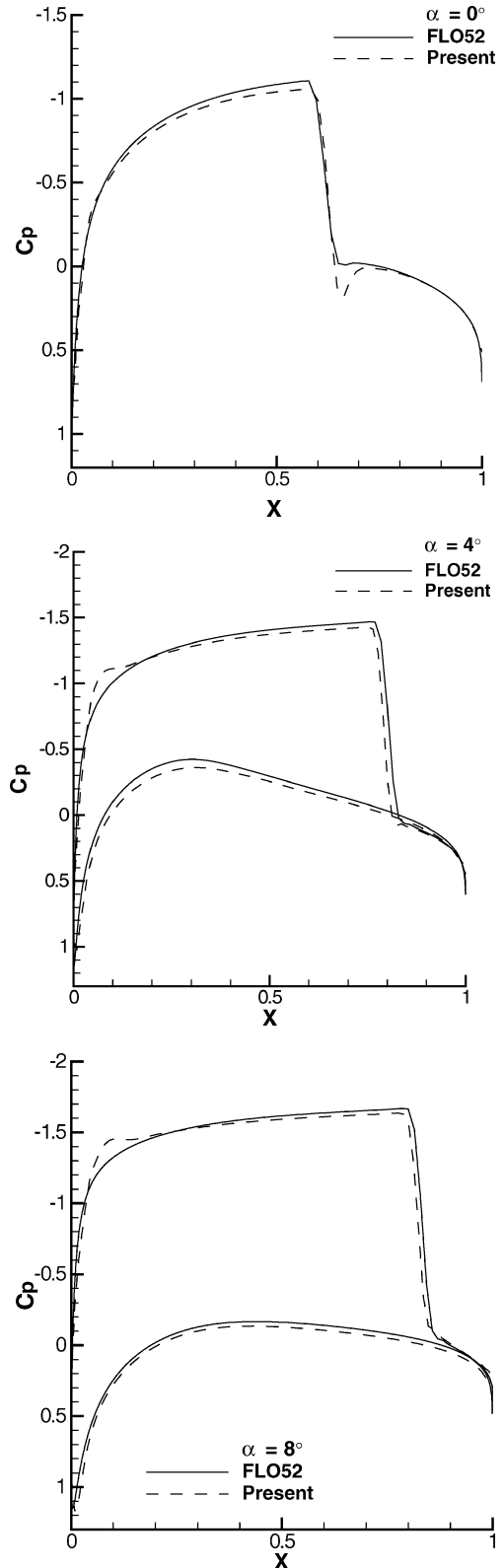


Fig. 3 Comparison of pressure distributions, NACA 0015: $M_\infty = 0.8$ and $\alpha = 0, 4,$ and 8 deg.

is seen that the present results agree well with those obtained by FLO52 even for the airfoil with a thickness ratio as large as 15% and angle of attack as large as 8 deg. When α is moderate and large, there appears a small bump in c_p on the upper surface in the region from $x = 0.05$ to 0.1 in the present solutions. This anomaly is caused by the leading-edge singularity problem discussed earlier. The truncation error in the approximate boundary conditions near the leading edge is proportional to the product of dy/dx , airfoil

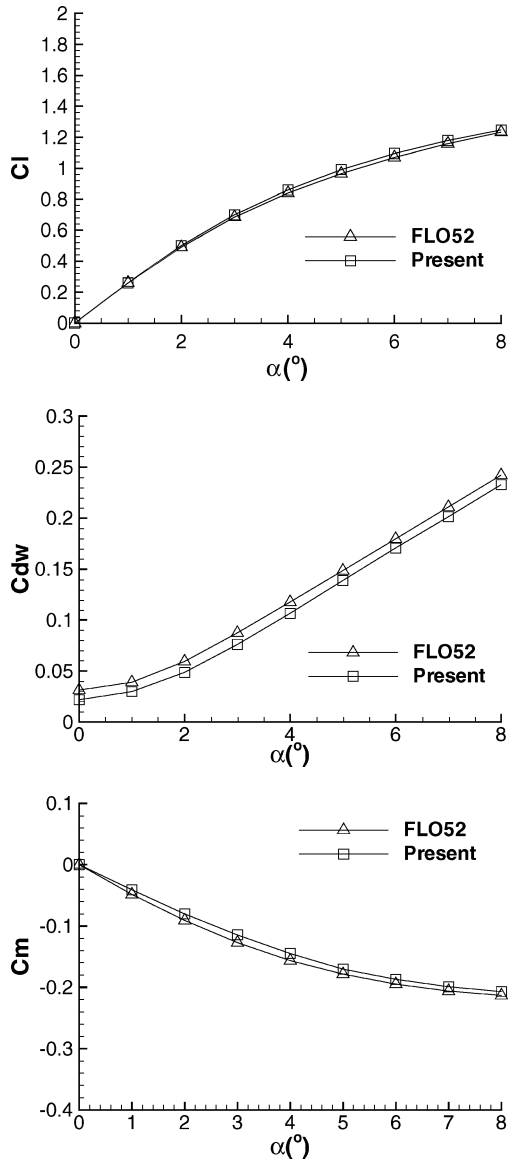


Fig. 4 Comparison of c_l , c_{dw} , and c_m , NACA 0015: $M_\infty = 0.8$ and $\alpha = 0 \sim 8$ deg.

thickness, and the gradient of the local flowfield. Therefore, the local errors are more pronounced for thicker airfoils at higher angles of attack where there is a greater gradient as a result of the suction peak on the top surface.

Figure 4 presents comparisons with FLO52 of the computed lift coefficient c_l , wave drag coefficient c_{dw} , and pitching-moment coefficient about quarter-chord c_m , vs α from 0 to 8 deg at $M_\infty = 0.8$ for the NACA 0015 airfoil. The relative errors of c_l , c_{dw} , and c_m are in general within 10%.

Computations for the NACA 0012 and NACA 0006 airfoils are also performed at the same $M_\infty = 0.8$ and $\alpha = 0-8$ deg conditions. Figure 5 shows the comparisons of the pressure distributions over the airfoil NACA 0012 at $\alpha = 0, 4,$ and 8 deg with those obtained by FLO52. Figure 6 gives the comparisons of c_l , c_{dw} , and c_m vs α from 0–8 deg for the same airfoil. The same plots of surface-pressure distribution and integrated lift, wave drag, and moment coefficients vs angle of attack for the NACA 0006 airfoil are shown in Figs. 7 and 8, respectively. The leading-edge pressure distribution anomaly is significantly reduced for the two thinner airfoils at the same angles of attack, which is expected because both dy/dx and the airfoil thickness are reduced.

At low angles of attack, the solutions of the approximate-boundary-condition method agree very well with those by FLO52. However, both Figs. 5 and 7 show that the present method predicts

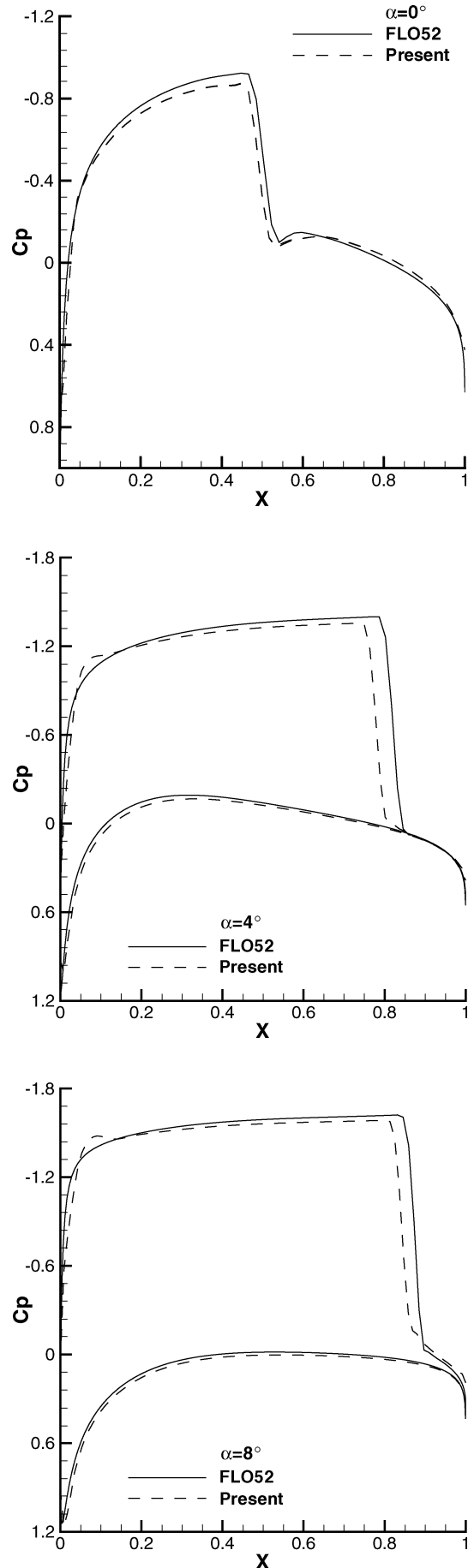


Fig. 5 Comparison of pressure distributions, NACA 0012: $M_\infty = 0.8$ and $\alpha = 0, 4,$ and 8 deg.

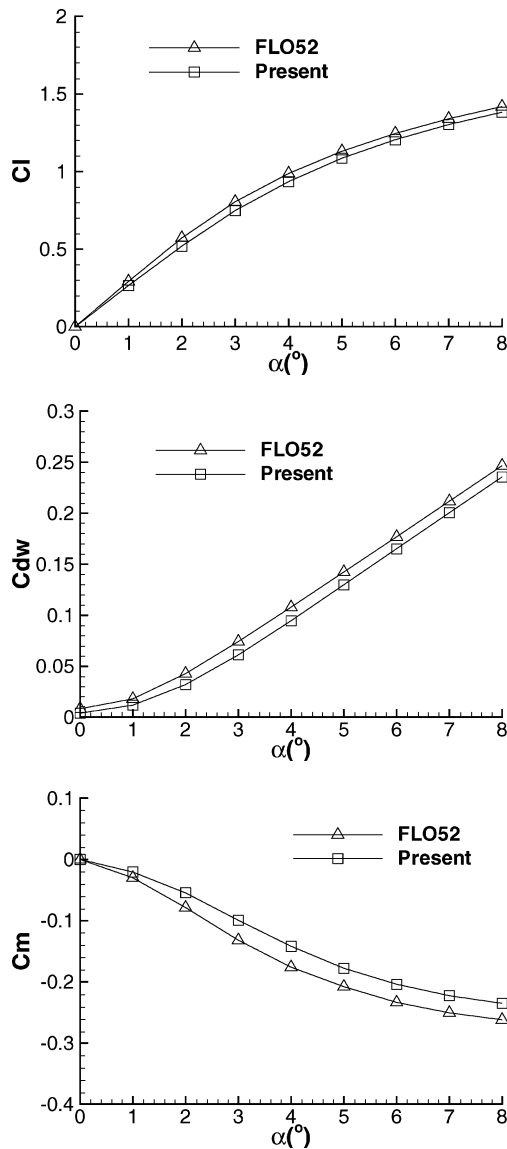


Fig. 6 Comparison of c_l , c_{dw} , and c_m , NACA 0012: $M_\infty = 0.8$ and $\alpha = 0 \sim 8$ deg.

shock waves that are noticeably forward compared to the results by FLO52 for the two thinner airfoils at higher angles of attack. This difference in shock position is responsible for the larger differences in the lift and moment coefficients at higher angles of attack as shown in Figs. 6 and 8. It is not clear what the exact reason is for this difference in shock position. Surprisingly, the shock positions predicted for the thicker NACA 0015 airfoil are accurate even at large angles of attack as shown in Fig. 3. Figures 5 and 7 show that the differences in shock location become significant when the shocks are strong and appear over the relatively flat surface of the thin airfoils near the trailing edge where shocks can be sensitive to slight errors in the boundary-condition treatment. In addition, a thin airfoil results in a larger suction peak, which also degrades the accuracy of the approximate boundary-condition method because of the increased gradient of the flowfield as discussed earlier. Implementation of a higher-order expansion in treating the boundary conditions might be able to improve the accuracy. Fortunately, even with the present implementation these differences are limited and do not increase further once the angle of attack is over 4 deg because the difference in shock location stays almost constant thereafter.

B. Unsteady Flows

The present approximate method is used to calculate the flow over an NACA 0012 airfoil pitching around its quarter-chord point.

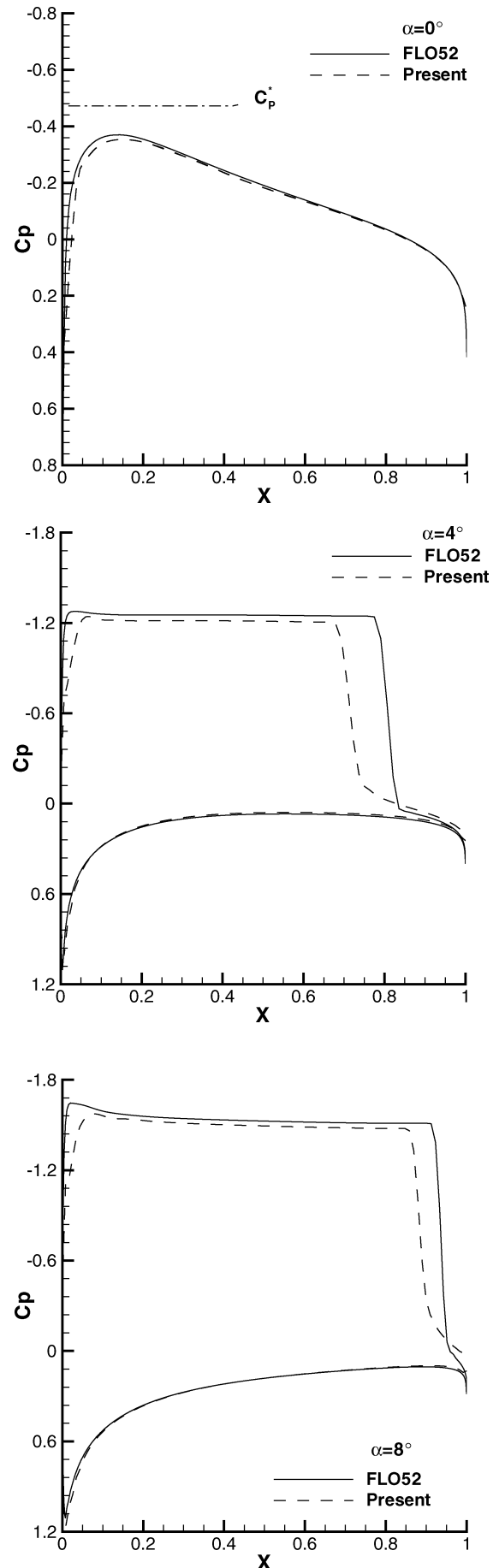


Fig. 7 Comparison of pressure distributions, NACA 0006: $M_\infty = 0.8$ and $\alpha = 0, 4$, and 8 deg.

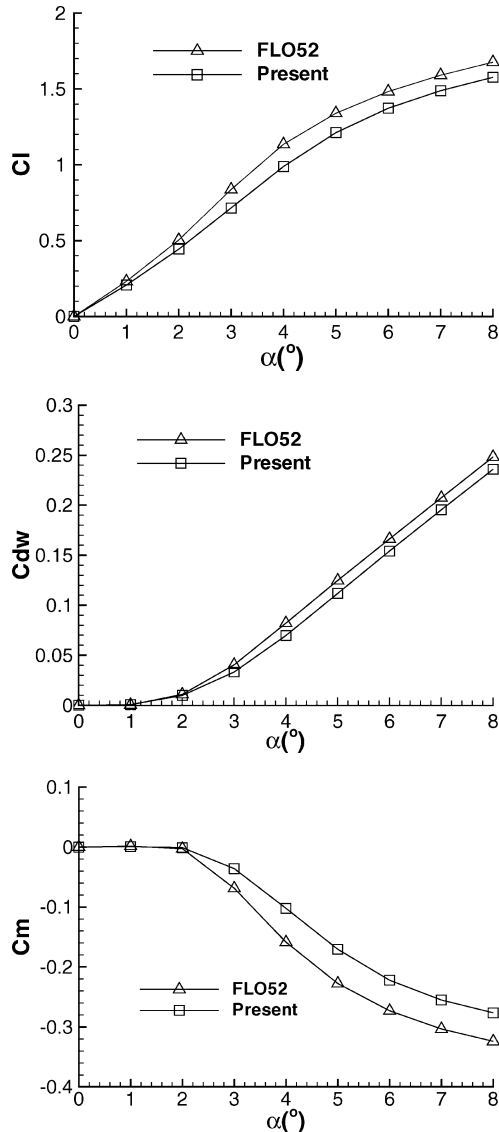


Fig. 8 Comparison of c_l , c_{dw} , and c_m , NACA 0012: $M_\infty = 0.8$ and $\alpha = 0 \sim 8$ deg.

Experimental data were provided by Landon.²⁶ The pitching motion of the airfoil is described by the following equation:

$$\alpha(t) = \alpha_m + \alpha_0 \sin \omega t \quad (32)$$

where ω , α_m , and α_0 are constants. The angular frequency ω is related to the reduced frequency defined as

$$\kappa = \omega c / 2U_\infty \quad (33)$$

The rectilinear grids used in the unsteady-flow calculations are the same as those used in the preceding steady-flow computations. The criterion for the convergence of the pseudotime computations is that the maximum magnitude of the residuals be reduced by more than four orders of magnitude. To satisfy this criterion, the number of the pseudotime steps within each real time step is usually 150. The calculations start from the uniform flow of velocity U_∞ as an initial solution. After three real-time cycles of the airfoil motion, an essentially periodic solution is obtained. In this paper six cycles of motion are used to ensure the computed results to be periodic.

The present approximate method is validated by comparing with results obtained by the Euler option of NS83.²³ Results are also compared with experimental data. The AGARD CT case 5 of Ref. 26 is studied. The airfoil is an NACA 0012 pitching at the freestream Mach number $M_\infty = 0.755$, $\alpha_m = 0.016$ deg, $\alpha_0 = 2.51$ deg, and $\kappa = 0.0814$. The experimental $Re = 5.5 \times 10^6$. The comparisons of the present inviscid computations and the experimental data of the

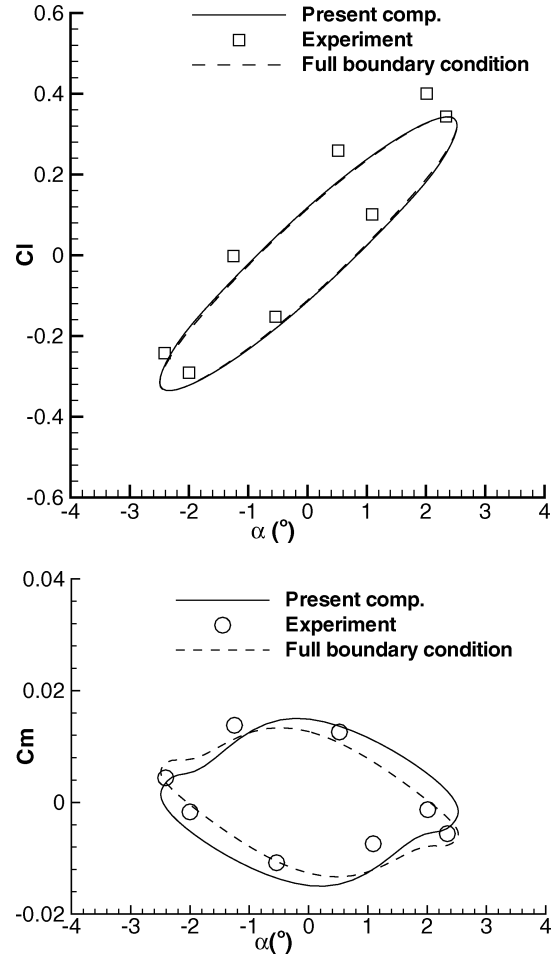


Fig. 9 Comparison of lift and moment coefficients by the present computation with approximate boundary conditions, Euler solution on body-fitted grid with full boundary conditions, and experiment, NACA 0012: $M_\infty = 0.755$, $\alpha_m = 0.016$ deg, $\alpha_0 = 2.51$ deg, and $\kappa = 0.0814$.

instantaneous lift and moment coefficients vs the instantaneous angle of attack are presented in Fig. 9. The computed instantaneous pressure distributions at the eight phase angles during the sixth cycle of motion are compared with the experimental data in Fig. 10. The eight phase angles are 25.3, 67.8, 127.4, 168.4, 210.3, 255.1, 306.6, and 347.2 deg. The time variation of the computed and experimental data of the surface-pressure distributions can be expressed in terms of their Fourier components. Figure 11 shows the comparison of the real and imaginary parts of the first three Fourier modes of the unsteady pressure coefficient over the airfoil surface. The solutions with the full boundary conditions in general give better resolution of the pressure distribution in the high suction areas and better shock positions than the solutions with the approximate boundary conditions compared to the experimental data. The solutions with the approximate boundary conditions show a slight bump when there is a large suction near the leading edge. This is seen in both Fig. 10 and the first Fourier mode of the unsteady pressure coefficient shown in Fig. 11. However, the overall agreement of the present solution with either the solution by the full boundary conditions or the experimental data are good. Batina²⁷ computed the Euler solutions with full boundary conditions on an unstructured body-fitted grid and compared his solutions with the same experimental data as we have done here. His computed results have qualitatively the same degree of agreement with the experimental data as do the computed results by the present methods.

C. Flutter Calculations

We use the current unsteady Euler solver in a coupled fluid-structure simulation method⁸ for the two-dimensional Isogai wing model,^{28,29} case A ($\mu = 60$). This model simulates the bending and

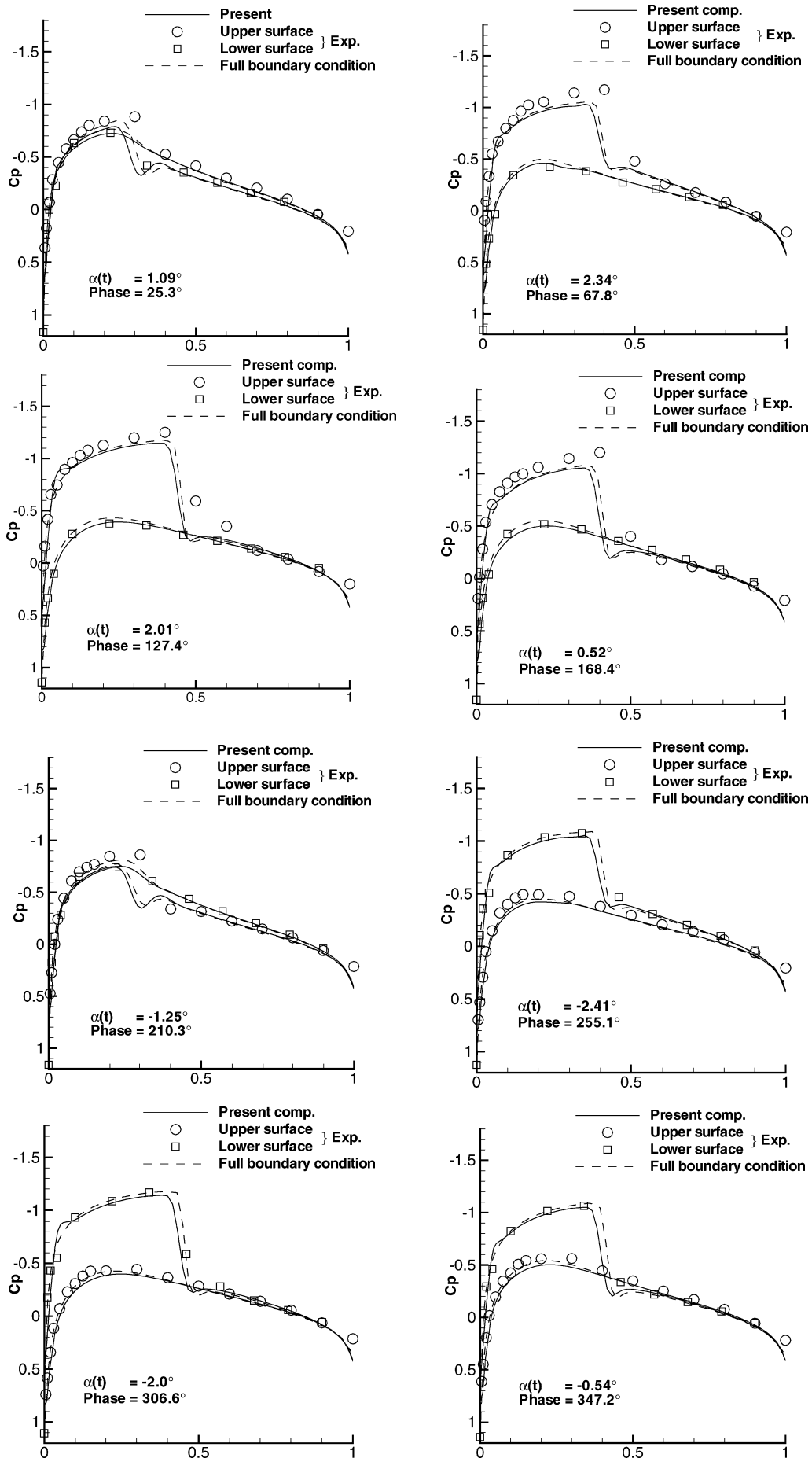


Fig. 10 Comparison of surface-pressure distributions by the present computation with approximate boundary conditions, Euler solution on body-fitted grid with full boundary conditions, and experiment, NACA 0012: $M_\infty = 0.755$, $\alpha_m = 0.016$ deg, $\alpha_0 = 2.51$ deg, and $\kappa = 0.0814$.

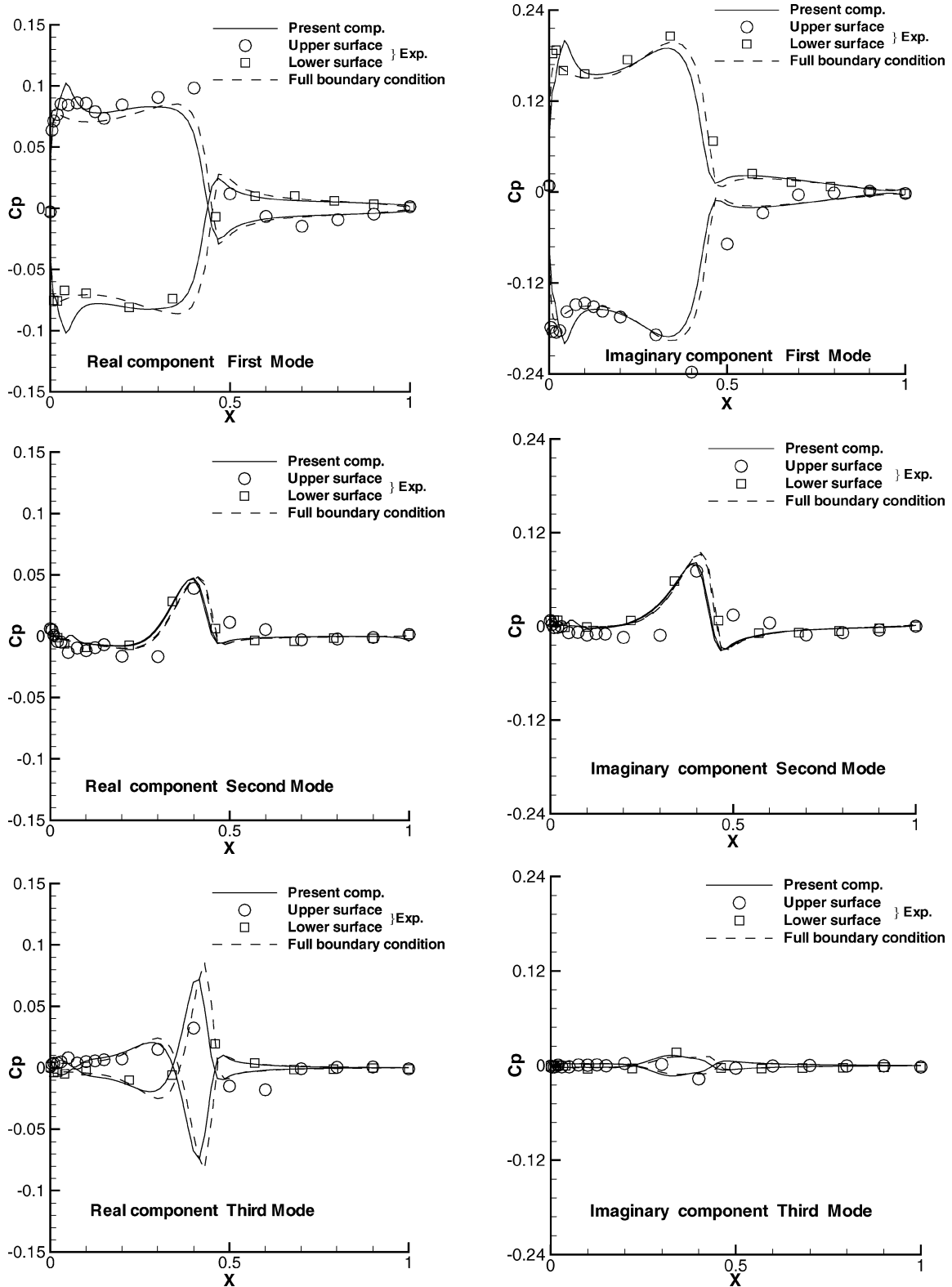


Fig. 11 Comparison of Fourier components of surface-pressure variations by the present computation with approximate boundary conditions, Euler solution on body-fitted grid with full boundary conditions, and experiment, NACA 0012: $M_\infty = 0.755$, $\alpha_m = 0.016$ deg, $\alpha_0 = 2.51$ deg, and $\kappa = 0.0814$.

torsional motion of a wing cross section in the outboard portion of a swept wing. It consists of two degrees of freedom, plunging and pitching, for a NACA 64A010 airfoil. We compute this case with the current Euler equations and compare the results in Ref. 8. The details of the structural model can be found in Ref. 30 as well as in Refs. 28 and 29.

Figures 12–14 show the flutter computational results for the Isogai wing model at a flight Mach number of 0.825. Plotted in the figures

are the time history of the pitching and plunging amplitude computed by the integrated fluid-structure simulation code with the current Euler solver. Figure 12 is a case with a low speed index $V_f = 0.530$. V_f is defined as

$$V_f = U_\infty / b\omega\sqrt{\mu}$$

where ω is the eigenfrequency of the structure. For this low V_f , Fig. 12 shows that both the pitching and plunging amplitude decays

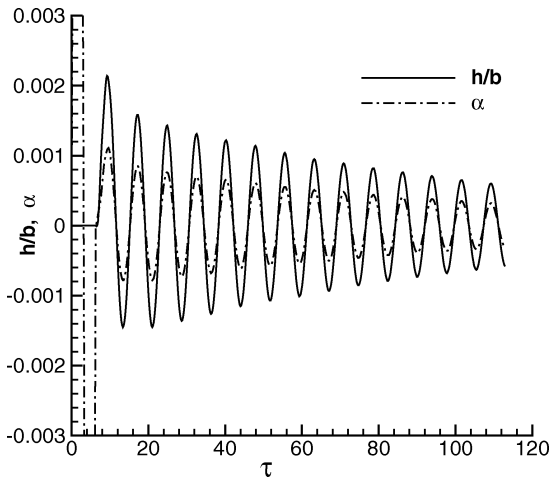


Fig. 12 Time history of pitching and plunging motion for the Isogai wing model for $M_\infty = 0.825$ and $V_f = 0.530$, stable situation.

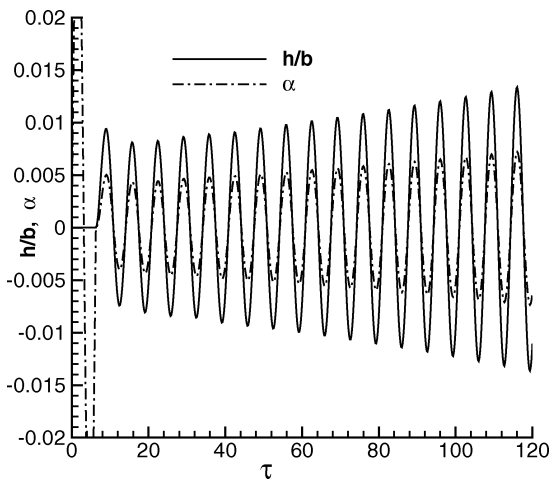


Fig. 13 Time history of pitching and plunging motion for the Isogai wing model for $M_\infty = 0.825$ and $V_f = 0.78$, unstable situation.

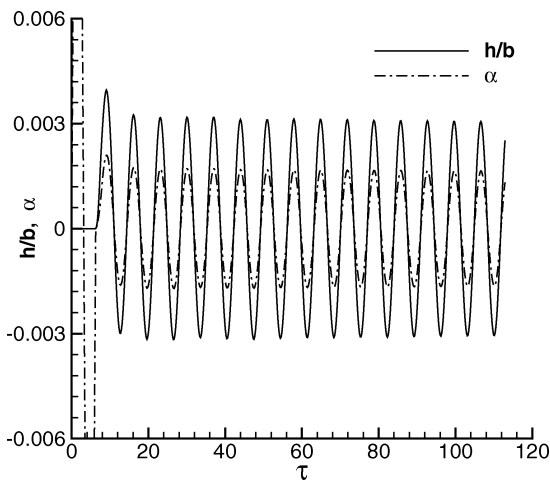


Fig. 14 Time history of pitching and plunging motion for the Isogai wing model for $M_\infty = 0.825$ and $V_f = 0.71$, neutral situation.

with time, indicating that the aeroelastic system is stable for this particular condition. At a higher V_f , the system can become less and less stable until one or both of the pitching and plunging motions diverge as shown in Fig. 13 when $V_f = 0.78$. In between these two V_f conditions, there is a particular point where the system is neutrally stable. This is shown in Fig. 14 when $V_f = 0.71$.

A converging point and a diverging point like the preceding are first identified, from which we can interpolate the V_f in between to

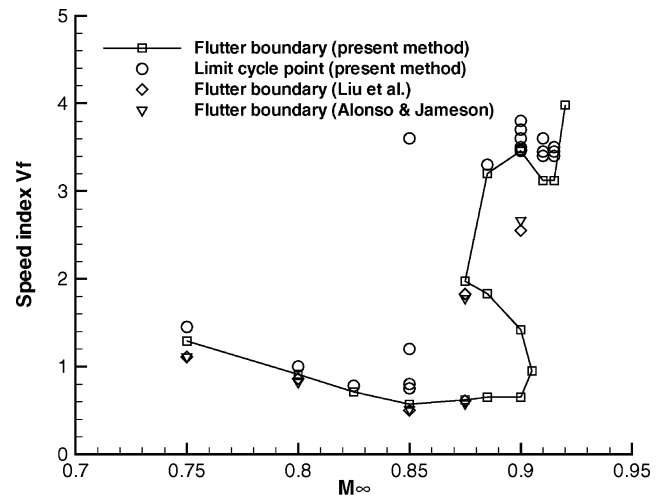


Fig. 15 Computed flutter boundary for the Isogai wing model case A.

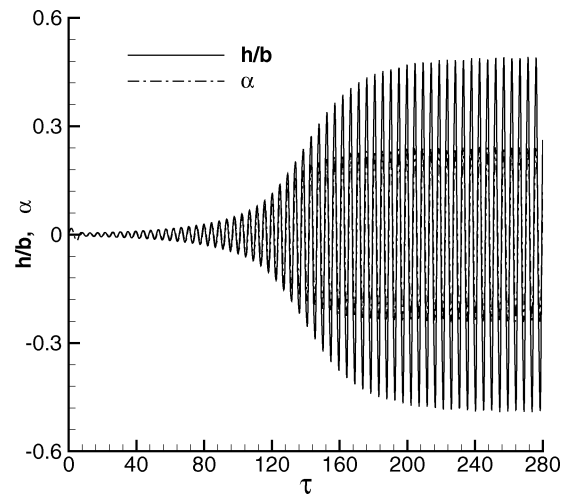


Fig. 16 Time history of pitching and plunging motion for the Isogai wing model case A for $M_\infty = 0.75$ and $V_f = 1.45$.

obtain an estimate of the neutral point. We then perform a computation with the new V_f to see if it is above or below the stability limit, or perhaps right at the neutral point. It might take several runs for a given freestream Mach number before the V_f corresponding to the neutral stability point can be accurately located by this bisection method. With this method computations for a number of freestream Mach numbers for the Isogai wing model are performed. The flutter boundary predicted by the present method on a Cartesian grid with the first-order approximate method is compared in Fig. 15 with those predicted by Liu et al.⁸ and Alonso and Jameson³⁰ both with the full boundary conditions. The agreement is good except for the point at $M_\infty = 0.9$, where the flutter boundary makes a turn as is shown in Fig. 15. The system is very sensitive near this critical point. A recent review paper by Dowell et al.¹⁷ also showed spread of data points near that point by other methods. Many runs are performed with the present approximate method to map out the details of the flutter boundary in the transonic range where the flutter boundary can curve back into the unstable region. For example, at $M_\infty = 0.885$ the system initially crosses the stability boundary at $V_f = 0.65$ to become unstable as V_f increases. As V_f increases above 1.83; however, the system becomes stable again until V_f reaches above 3.20 when it returns to being unstable. Although a complete map of the flutter boundary is computed and presented by the present method in Fig. 15, detailed examination of the flow near the $M_\infty = 0.9$ critical point and comparison with other methods are needed in a future effort.

Despite the use of the first-order approximate boundary conditions, the code is also able to simulate LCO. Figure 16 shows such a

case at $M_\infty = 0.75$ and $V_f = 1.45$ for the same Isogai wing case. For each flight Mach number, the code predicts LCO when V_f is sufficiently large after it crosses the flutter boundary. The circles shown in Fig. 15 mark such conditions predicted by the present computations. It is, however, not clear whether such predictions are reliable because the computations are based on an inviscid model and also with the approximate boundary conditions. Dowell et al. discuss in a recent review paper¹⁷ the significance of including viscous effects for LCO predictions and cite in particular LCO predictions for the Isogai wing case. An interactive boundary-layer method like the one used in CAP-TSD can be used to improve the accuracy of the model.

VI. Conclusions

This paper presents a numerical method for solving the steady and unsteady Euler equations on stationary Cartesian grids. It is shown that the boundary conditions on the surface of an airfoil can be approximated by their first-order expansions on the mean position of the airfoil chord while the full Euler equations are solved in the flowfield on stationary non-body-conforming Cartesian type of grids. Although the thickness of the airfoil and the unsteady deformation are required to be small because of the first-order expansion of the boundary conditions in terms of the surface displacement from its mean positions, the mean angle of attack is not formally under the small perturbation restriction in terms of order of accuracy. In practice, however, the mean angle of attack might be limited because the truncation error in the approximate boundary conditions increases as a result of increased flow gradients caused by strong suction peaks at high angles of attack.

For steady transonic flows, the calculated pressure distributions, lift coefficients, wave-drag coefficients, and pitching-moment coefficients by the approximate method in general agree well with the solutions of FLO52 using body-conforming curvilinear grids for airfoils of thickness ratios up to 15% and angle of attack up to 8 deg.

For unsteady flows, the calculated instantaneous lift, moment, surface-pressure distributions, and the Fourier components of the surface-pressure variations by the approximate method agree well with those obtained on body-fitted grids with full boundary conditions and the experimental data for the NACA 0012 airfoil with oscillating pitch angles up to 3 deg at transonic speeds.

The unsteady flow solver is used in time-domain coupled fluid-structure simulations of airfoil flutter. The computed flutter boundary by the present method on a Cartesian grid with approximate boundary conditions are in good agreement with results by Euler solvers on body-fitted grids with full boundary conditions for the Isogai wing model. The method is also found to simulate limit-cycle oscillations (LCO) solutions although the LCO amplitude might not be reliable with the assumed approximate boundary conditions. The advantage of using a single stationary non-body-conforming rectangular grid opens the door for the efficient computation of unsteady fluid-structure interaction problems involving slightly deforming airfoils or wings of small thickness by using the present approximate boundary condition method. Further studies will include extension to three dimensions and the use of an interactive boundary layer method to account for viscous effects.

Acknowledgment

This work is supported by the NASA Langley Research Center, Contract NAG-1-02050.

References

- ¹Albano, E., and Rodden, W. P., "A Doublet Lattice Method for Calculating Lift Distributions on Oscillating Surfaces in Subsonic Flows," *AIAA Journal*, Vol. 7, No. 2, 1969, pp. 279–285.
- ²Lee-Rausch, E. M., and Batina, J. T., "Wing Flutter Boundary Prediction Using Unsteady Euler Aerodynamic Method," *Journal of Aircraft*, Vol. 32, No. 2, 1995, pp. 416–422.
- ³Lee-Rausch, E. M., and Batina, J. T., "Wing Flutter Computations Using an Aerodynamic Model Based on the Navier–Stokes Equations," *Journal of*

Aircraft, Vol. 33, No. 6, 1996, pp. 1139–1147.

⁴Gibbons, M., "Aeroelastic Calculations Using CFD for a Typical Business Jet Model," NASA CR 4753, Sept. 1996.

⁵Tang, L., Bartels, R., Chen, P., and Liu, D. D., "Numerical Investigation of Transonic Limit Oscillations of a 2-D Supercritical Wing," AIAA Paper 2001-1290, April 2001.

⁶Byun, C., and Guruswamy, G. P., "Aeroelastic Computation on Wing-Body-Control Configurations on Parallel Computers," *Journal of Aircraft*, Vol. 35, No. 2, 1998, pp. 288–294.

⁷Goodwin, S. A., Weed, R. A., Sankar, L. N., and Raj, P., "Toward Cost-Effective Aeroelastic Analysis on Advanced Parallel Computing Systems," *Journal of Aircraft*, Vol. 36, No. 4, 1999, pp. 710–715.

⁸Liu, F., Cai, J., Zhu, Y., Wong, A. S. F., and Tsai, H.-M., "Calculation of Wing Flutter by a Coupled Fluid-Structure Method," *Journal of Aircraft*, Vol. 38, No. 2, 2001, pp. 334–342.

⁹Gordner, R. E., and Melville, R. B., "Numerical Simulation of Limit-Cycle Oscillations of a Cropped Delta Wing Using the Full Navier–Stokes Equations," *International Journal of Computational Fluid Dynamics*, Vol. 14, No. 3, 2001, pp. 211–224.

¹⁰Raveh, D. E., Levy, Y., and Karpel, M., "Efficient Aeroelastic Analysis Using Computational Unsteady Aerodynamics," *Journal of Aircraft*, Vol. 38, No. 3, 2001, pp. 547–556.

¹¹Schewe, G., Mai, H., and Dietz, G., "Nonlinear Effects in Transonic Flutter with Emphasis in Manifestations of Limit Cycle Oscillations," *Journal of Fluids and Structures*, Vol. 18, No. 1, 2003, pp. 3–22.

¹²Beran, P., and Silva, W., "Reduced-Order Modeling: New Approaches for Computational Physics," AIAA Paper 2001-0853, Jan. 2001.

¹³Geuzaine, P., Brown, G., Harris, C., and Farhat, C., "Aeroelastic Dynamic Analysis of a Full F-16 Configuration for Various Flight Conditions," *AIAA Journal*, Vol. 41, No. 3, 2003, pp. 363–371.

¹⁴Harris, T. M., and Huttshell, L. J., "Aeroelasticity Research at Wright–Patterson Air Force Base (Wright Field) from 1953–1993," *Journal of Aircraft*, Vol. 40, No. 5, 2003, pp. 813–819.

¹⁵Yurkovich, R., "Status of Unsteady Aerodynamic Prediction for Flutter of High-Performance Aircraft," *Journal of Aircraft*, Vol. 40, No. 5, 2003, pp. 832–842.

¹⁶Schuster, D. M., Liu, D. D., and Huttshell, L. J., "Computational Aeroelasticity: Success, Progress, Challenge," *Journal of Aircraft*, Vol. 40, No. 5, 2003, pp. 843–856.

¹⁷Dowell, E., Edwards, J., and Strganac, T., "Nonlinear Aeroelasticity," *Journal of Aircraft*, Vol. 40, No. 5, 2003, pp. 857–874.

¹⁸Bartels, R., "Flow and Turbulence Modeling and Computation of Shock Buffet Onset for Conventional and Supercritical Airfoils," NASA TP 1998-206908, Feb. 1998.

¹⁹Batina, J. T., "A Finite-Difference Approximate-Factorization Algorithm for Solution of the Unsteady Transonic Small-Disturbance Equation," NASA TP 3129, Jan. 1992.

²⁰Edwards, J., "Transonic Shock Oscillations Calculated with a New Interactive Boundary Layer Coupling Method," AIAA Paper 93-0777, Jan. 1993.

²¹Edwards, J., "Transonic Shock Oscillations and Wing Flutter Calculated with an Interactive Boundary Layer Coupling Method," NASA TM-110284, Aug. 1996.

²²Jameson, A., Schmidt, W., and Turkel, E., "Numerical Solutions of the Euler Equations by Finite Volume Methods Using Runge–Kutta Time-Stepping Schemes," AIAA Paper 81-1259, June 1981.

²³Liu, F., and Ji, S., "Unsteady Flow Calculations with a Multigrid Navier–Stokes Method," *AIAA Journal*, Vol. 34, No. 10, 1996, pp. 2047–2053.

²⁴Jameson, A., "Time Dependent Calculations Using Multigrid, with Applications to Unsteady Flows past Airfoils and Wings," AIAA Paper 91-1596, June 1991.

²⁵Gao, C., Luo, S., and Liu, F., "Numerical Solution of the Unsteady Euler Equations for Airfoils Using Approximate Boundary Conditions," *Acta Mechanica Sinica*, Vol. 19, No. 5, 2003, pp. 427–436.

²⁶Landon, R. H., "NACA 0012 Oscillating and Transient Pitching, Compendium of Unsteady Aerodynamic Measurements, Data Set 3," AGARD, Rept. R-702, Aug. 1982.

²⁷Batina, J. T., "Unsteady Euler Airfoil Solutions Using Unstructured Dynamic Meshes," *AIAA Journal*, Vol. 28, No. 8, 1990, pp. 1381–1388.

²⁸Isogai, K., "On the Transonic-Dip Mechanism of Flutter of a Sweptback Wing," *AIAA Journal*, Vol. 17, No. 7, 1979, pp. 793–795.

²⁹Isogai, K., "On the Transonic-Dip Mechanism of Flutter of a Sweptback Wing: Part II," *AIAA Journal*, Vol. 19, No. 9, 1981, pp. 1240–1242.

³⁰Alonso, J. J., and Jameson, A., "Fully-Implicit Time-Marching Aeroelastic Solutions," AIAA Paper 94-0056, Jan. 1994.